

## RESEARCH ARTICLE

10.1002/2013JD020483

## Special Section:

Suomi NPP Calibration and Validation Scientific Results

## Key Points:

- First flight unit performing well
- On-orbit evaluations of ATMS performance are presented

## Correspondence to:

E. Kim,  
ed.kim@nasa.gov

## Citation:

Kim, E., C.-H. J. Lyu, K. Anderson, R. V. Leslie, and W. J. Blackwell (2014), S-NPP ATMS instrument prelaunch and on-orbit performance evaluation, *J. Geophys. Res. Atmos.*, 119, 5653–5670, doi:10.1002/2013JD020483.

Received 1 JUL 2013

Accepted 22 MAR 2014

Accepted article online 27 MAR 2014

Published online 13 MAY 2014

## S-NPP ATMS instrument prelaunch and on-orbit performance evaluation

Edward Kim<sup>1</sup>, Cheng-Hsuan J. Lyu<sup>2</sup>, Kent Anderson<sup>3</sup>, R. Vincent Leslie<sup>4</sup>, and William J. Blackwell<sup>4</sup>
<sup>1</sup>NASA Goddard Space Flight Center, Greenbelt, Maryland, USA, <sup>2</sup>IM. Systems Group at NASA Goddard Space Flight Center, Greenbelt, Maryland, USA, <sup>3</sup>Northrop Grumman Electronic Systems, Azusa, California, USA, <sup>4</sup>MIT Lincoln Laboratory, Lexington, Massachusetts, USA

**Abstract** The first of a new generation of microwave sounders was launched aboard the Suomi-National Polar-Orbiting Partnership satellite in October 2011. The Advanced Technology Microwave Sounder (ATMS) combines the capabilities and channel sets of three predecessor sounders into a single package to provide information on the atmospheric vertical temperature and moisture profiles that are the most critical observations needed for numerical weather forecast models. Enhancements include size/mass/power approximately one third of the previous total, three new sounding channels, the first space-based, Nyquist-sampled cross-track microwave temperature soundings for improved fusion with infrared soundings, plus improved temperature control and reliability. This paper describes the ATMS characteristics versus its predecessor, the advanced microwave sounding unit (AMSU), and presents the first comprehensive evaluation of key prelaunch and on-orbit performance parameters. Two-year on-orbit performance shows that the ATMS has maintained very stable radiometric sensitivity, in agreement with prelaunch data, meeting requirements for all channels (with margins of ~40% for channels 1–15), and improvements over AMSU-A when processed for equivalent spatial resolution. The radiometric accuracy, determined by analysis from ground test measurements, and using on-orbit instrument temperatures, also shows large margins relative to requirements (specified as <1.0 K for channels 1, 2, and 16–22 and <0.75 K for channels 3–15). A thorough evaluation of the performance of ATMS is especially important for this first proto-flight model unit of what will eventually be a series of ATMS sensors providing operational sounding capability for the U.S. and its international partners well into the next decade.

## 1. Introduction

The first Advanced Technology Microwave Sounder (ATMS) proto flight model (PFM) unit was launched by NASA on 28 October 2011 on the Suomi-National Polar-Orbiting Partnership (S-NPP) satellite for NOAA. It was placed into an 824 km, polar Sun-synchronous, 16 day-repeat-cycle orbit with a local ascending node equator crossing time of 13:30. As the first S-NPP instrument fully activated, ATMS provided the first-light image shown in Figure 1, which is also the first-light image for the entire Joint Polar Satellite System (JPSS) program.

ATMS works in conjunction with the Cross-Track Infrared Sounder (CrIS) to form the Cross-Track Infrared and Microwave Sounder Suite (CrIMSS). CrIMSS observations are used to generate two key performance parameters (KPPs)—atmospheric vertical moisture profile (AVMP) and atmospheric vertical temperature profile (AVTP). From these two products, a third environmental data record (EDR, equivalent to NASA “level 2” data), the atmospheric vertical pressure profile, is also calculated. AVTP and AVMP are needed in both clear and cloudy conditions. For further information, see the Joint Polar Satellite System Algorithm Theoretical Basis Document (ATBD) for the CrIS, volume II, environmental data records.

Heritage sounders had found “the limiting effects of cloud contamination in the field of view of the infrared (IR) sounder,” but “microwave data are not affected by most clouds [Aumann *et al.*, 2003].” Unfortunately, “the vertical resolution achievable in the troposphere from the microwave region is inferior to that achievable in the 4.3  $\mu\text{m}$  CO<sub>2</sub> band [Aumann *et al.*, 2003].” However, in areas classified as overcast, no IR retrieval is performed, and AVTP and AVMP products are derived exclusively from microwave ATMS measurements [Joint Polar Satellite System Algorithm Theoretical Basis Document Cross-Track Infrared Sounder Environmental Data Record, 2010].

Analyses using previous generation IR and microwave sensors (Atmospheric Infrared Sounder (AIRS) and advanced microwave sounding unit (AMSU), respectively) have shown a substantially positive impact to

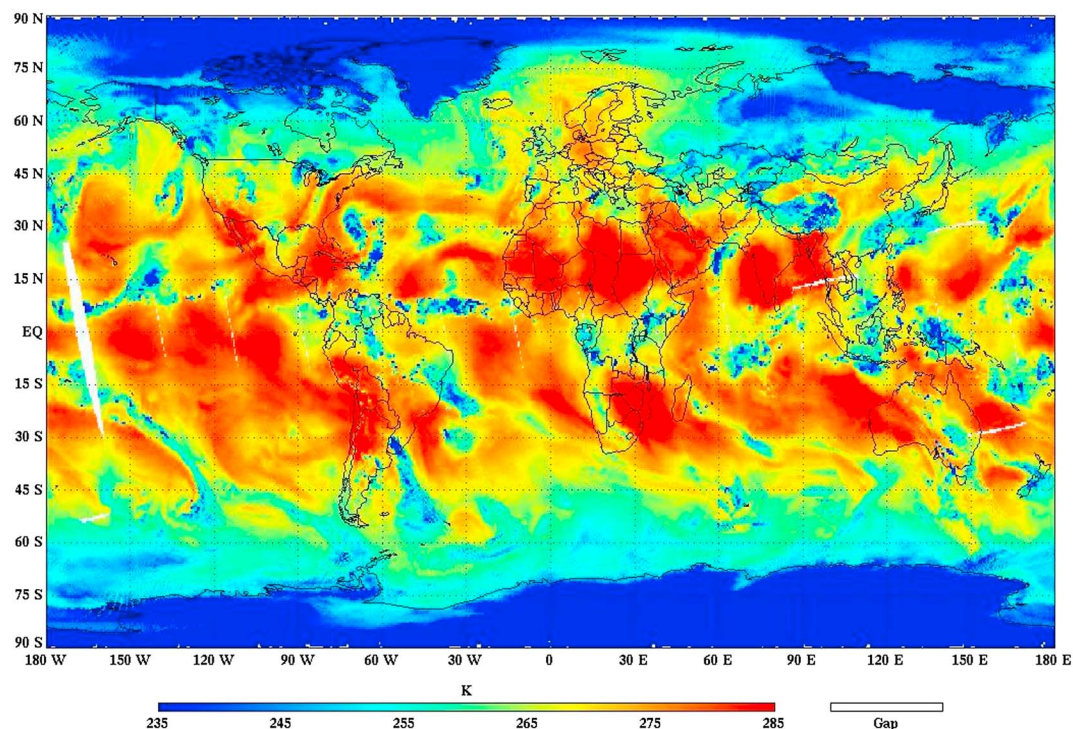


**Figure 1.** The first light image for the JPSS program was from ATMS, showing channel 18 (183.3 GHz) antenna temperature on 8 November 2011. (Image generated by NOAA/Center for Satellite Applications and Research.)

forecast accuracy when the radiances are assimilated into numerical weather prediction models. Microwave radiances in particular are among the highest impact observations used by operational numerical weather prediction (NWP) forecast models [Cardinali, 2009].

The following ATMS data products are available to users. Raw data records (RDRs, equivalent to NASA “level 1A” data) constitute time-stamped, raw or unprocessed sensor data, e.g., radiometric counts. The RDRs have the data necessary to calibrate the radiometric data or convert the telemetry, but the calibration and conversions are not applied. The temperature data record (TDR, no equivalent NASA data level) constitutes calibrated antenna temperatures that have been geolocated to the ATMS 96 fields of view (FOVs). The sensor data records (SDRs, equivalent to NASA “level 1B” data) contain the brightness temperatures. The final ATMS data product is the remapped ATMS SDR. In the remapped SDR, a predetermined number of ATMS SDR FOVs have been remapped to match the CrIS 30 fields of regard (FORs) using a Backus-Gilbert resampling routine [Poe, 1990; CrIS EDR ATBD]. In this paper, we present evaluations of selected on-orbit performance parameters, including comparisons with prelaunch performance data where appropriate. The paper is organized into four major sections: a brief description of the ATMS instrument and its spatial and spectral characteristics [Muth et al., 2005], detailed evaluations of on-orbit performance, and then a summary and a short description of future work.

## 2. Description

The Advanced Technology Microwave Sounder was developed by Northrop Grumman Electronic Systems (formerly Aerojet) under a NASA contract, for the S-NPP program. ATMS was specified to provide essentially the same data products as the prior AMSU-A and Microwave Humidity Sounder (MHS) instruments (primarily atmospheric temperature and humidity sounding) but with the following enhancements:

1. Faster scan rate and sampling rate, providing spatial Nyquist sampling of temperature sounding channels, permits more accurate resampling to CrIS footprints and hence supports more accurate retrievals from the fusion of ATMS and CrIS data
2. Additional sounding channels

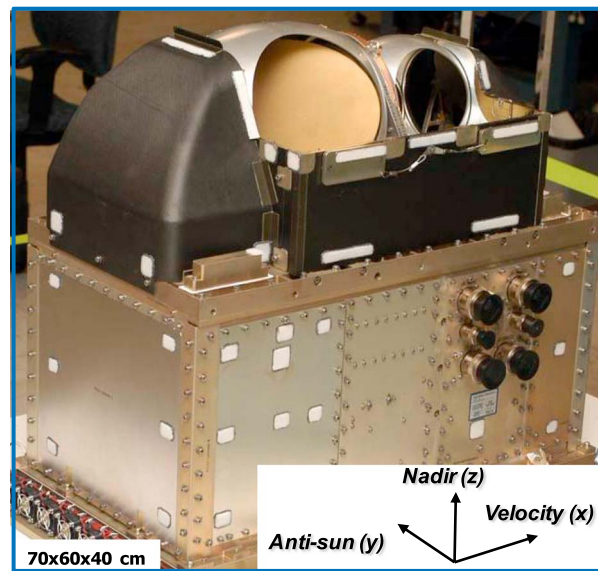


**Figure 2.** S-NPP ATMS instrument. (Photo courtesy of NGES.)

3. Thermal control via spacecraft cold plate to provide more flexibility for mounting location
4. Improved torque disturbance compensation
5. Improved reliability and longer life, due to significantly increased redundancies. ATMS predicted reliability is 0.795 at 7 years for channels 3–22; AMSU-A predicted reliability, using the same modeling methodology, was 0.771 at only 3 years for channels 3–14
6. Reduced size, weight, and power, relative to the heritage sensor suite
7. Wider swath width than AMSU, eliminates nearly all gaps in global coverage

In addition to the above listed improvements, ATMS provides better noise equivalent delta temperature (NE $\Delta$ T) performance than AMSU-A, when processed for equivalent spatial

resolution [Kleespies, 2007a], and improved linearity (based on ground test data). It has also been found that the use of the spacecraft heat rejection system results in improved temperature stability and consequent radiometric gain stability. Figure 2 is a view of ATMS from the sunside, showing the two scanning antenna apertures and the interface connector panel. A functional block diagram is shown in Figure 3. The ATMS sensor is an “integrate-while-scan” total-power-radiometer, with 96 FOVs per scan sweep covering the frequency range of 23.8 GHz to 190 GHz (in 22 channels). The ATMS scan period of 8/3 s is synchronized to the CrIS instrument scan. Two calibration looks are collected with each scan. They include viewing an internal calibration target (warm load) and viewing deep space (cold load) to provide two known temperature reference points for calibration. The temperature of the warm calibration load is monitored by platinum resistance thermometers to provide accurate warm load temperature readout.

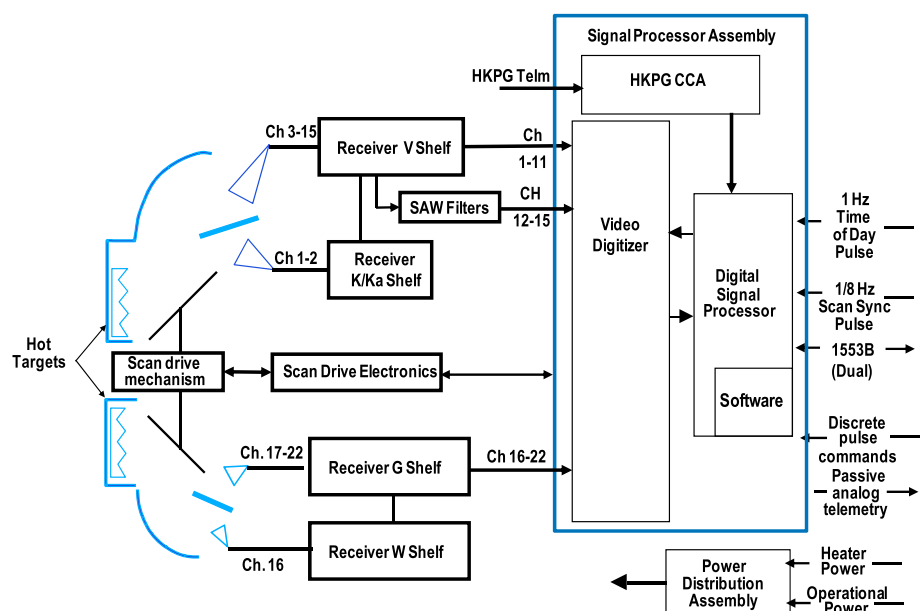


**Figure 3.** Simplified ATMS block diagram.

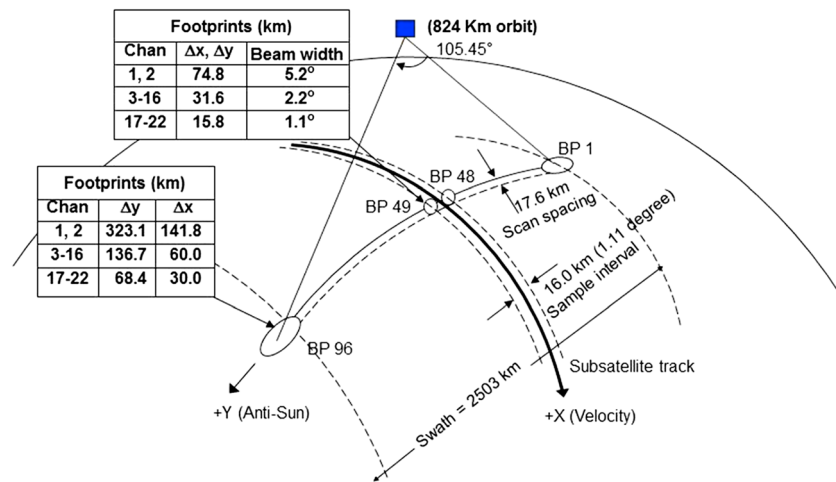


**Figure 4.** Ground swath and footprint geometry; “BP” is beam position.

The scanning geometry, swath width, and footprint dimensions are illustrated in Figure 4. The channels and spectral characteristics are shown in Tables 1a and 1b, which also identify the corresponding nearest AMSU-A, -B channels and the specified radiometric sensitivities ( $NE\Delta Ts$ ). Channel polarizations are identified as QV (quasi vertical), which means the polarization is in the Y-Z (across-track) scanning plane when in the nadir-pointing scan position or QH (quasi horizontal), for which the polarization is normal to the Y-Z plane, in the nadir-pointing position. Note that the direction  $-Y$  faces the Sun and Z points to nadir.

Tables 2a and 2b provide comparisons of antenna beam widths and spatial sampling for ATMS versus the predecessor sensors AMSU and MHS. It can be seen that the AMSU/MHS beam widths are smaller (better) for the 23/31 and 89 GHz channels, but ATMS has better spatial resolution for the 50–60 GHz band. Also, the ATMS provides substantially finer spatial sampling for the temperature sounding channels, which enables

**Table 1a.** ATMS Spectral Characteristics and Equivalent Channels on Precursor AMSU-A, -B, and MHS Sensors

ATMS Channel	AMSU-A, -B (MHS) Channel	Center Frequency (GHz)	Single Sideband (SSB) or Double Sideband (DSB)	Predetection Bandwidth (MHz)
1	1	23.8	SSB	270
2	2	31.4	SSB	180
3	3	50.3	SSB	180
4		51.76	SSB	400
5	4	52.8	SSB	400
6	5	53.596 $\pm$ 0.115	DSB	170
7	6	54.4	SSB	400
8	7	54.94	SSB	400
9	8	55.5	SSB	330
10	9	57.290,344	DSB	155
11	10	57.290,344 $\pm$ 0.217	DSB	78
12	11	57.290,344 $\pm$ 0.3,222 $\pm$ 0.048	DSB	36
13	12	57.290,344 $\pm$ 0.3,222 $\pm$ 0.022	DSB	16
14	13	57.290,344 $\pm$ 0.3,222 $\pm$ 0.010	DSB	8
15	14	57.290344 $\pm$ 0.3222 $\pm$ 0.0045	DSB	3
16	15 and 16 (H1)	88.2	SSB	2,000
17		165.5	DSB	1,150
	17 (H2)	150 (157)	DSB	1,000 (1,400)
18	20 (H5)	183.31 $\pm$ 7.0	DSB	
19		183.31 $\pm$ 4.5	DSB	2,000
20	19 (H4)	183.31 $\pm$ 3.0	DSB	1,000
21		183.31 $\pm$ 1.8	DSB	1,000
22	18 (H3)	183.31 $\pm$ 1.0	DSB	500



**Table 1b.** ATMS Sensitivity and Antenna Performance Parameters (From Ground Test Measurements)

ATMS Channel	NE $\Delta$ T (K) <sup>b</sup>		Polarization	Beam Width (Degrees)	
	Req't <sup>a</sup>	Measured <sup>c</sup>		Req't <sup>a</sup>	Measured <sup>c</sup>
1	$\leq 0.50$	0.25	QV	$5.2 \pm 0.52$	5.32–5.51
2	$\leq 0.60$	0.31	QV	$5.2 \pm 0.52$	5.23–5.60
3	$\leq 0.70$	0.37	QH	$2.2 \pm 0.22$	2.26–2.31
4	$\leq 0.50$	0.28	QH	$2.2 \pm 0.22$	2.27–2.34
5	$\leq 0.50$	0.28	QH	$2.2 \pm 0.22$	2.30–2.32
6	$\leq 0.50$	0.29	QH	$2.2 \pm 0.22$	2.23–2.31
7	$\leq 0.50$	0.27	QH	$2.2 \pm 0.22$	2.20–2.30
8	$\leq 0.50$	0.27	QH	$2.2 \pm 0.22$	2.25–2.32
9	$\leq 0.50$	0.29	QH	$2.2 \pm 0.22$	2.24–2.30
10	$\leq 0.75$	0.43	QH	$2.2 \pm 0.22$	2.20–2.23
11	$\leq 1.00$	0.56	QH	$2.2 \pm 0.22$	2.20–2.23
12	$\leq 1.00$	0.59	QH	$2.2 \pm 0.22$	2.20–2.23
13	$\leq 1.50$	0.86	QH	$2.2 \pm 0.22$	2.20–2.23
14	$\leq 2.20$	1.23	QH	$2.2 \pm 0.22$	2.20–2.23
15	$\leq 3.60$	1.95	QH	$2.2 \pm 0.22$	2.20–2.23
16	$\leq 0.30$	0.29	QV	$2.2 \pm 0.22$	2.04–2.26
17	$\leq 0.60$	0.46	QH	$1.1 \pm 0.11$	1.15–1.19
18	$\leq 0.80$	0.38	QH	$1.1 \pm 0.11$	1.07–1.17
19	$\leq 0.80$	0.46	QH	$1.1 \pm 0.11$	1.07–1.17
20	$\leq 0.80$	0.54	QH	$1.1 \pm 0.11$	1.07–1.17
21	$\leq 0.80$	0.59	QH	$1.1 \pm 0.11$	1.07–1.17
22	$\leq 0.90$	0.73	QH	$1.1 \pm 0.11$	1.07–1.17

<sup>a</sup>“Req’t” refers to requirement values.<sup>b</sup>NE $\Delta$ Ts in this table are for each ATMS beam position sample. For comparison with AMSU, the values here for channels 1–15 must be divided by  $\sqrt{9}=3$ , since there are nine ATMS samples corresponding to one AMSU sample at those frequencies.<sup>c</sup>“Measured” refers to actual measured values.

accurate remapping [Poe, 1990; CrIS EDR ATBD] to match the CrIS footprints, for improved CrIMSS products. Table 2b also indicates the wider ATMS swath width, which provides almost gap-free global coverage.

The primary contributors to radiometric calibration errors are the errors in hot calibration and cold calibration and nonlinearity of the transfer function. Hot calibration error sources are due to target emissivity, physical temperature measurement uncertainties, thermal gradients within the target, and radiometric leakage when viewing the target. Cold calibration errors are due to the Rayleigh approximation for cold space radiation and the antenna sidelobe intercepts with the Earth and the spacecraft. Table 3 provides the proposed bias offsets to compensate for these errors and the predicted random errors. The cold-calibration offset is the mean value of predicted cold calibration errors, and the random error is the residual 1 sigma deviation from the mean offset. For the hot calibration, the offset is one half of the worst-case predicted static errors (emissivity and leakage), and the random error is the root-sum-square (RSS) of the other (dynamic) error sources. In the overall accuracy predictions (Figure 5), the residual hot-calibration static error (after offset correction) was added to the RSS of all dynamic errors, which includes cold-calibration offset, nonlinearities, and drifts.

**Table 2a.** Beam Width (Degrees) Comparison of ATMS and AMSU/MHS

	ATMS	AMSU/MHS
23/31 GHz	5.2	3.3
50–60 GHz	2.2	3.3
89–GHz	2.2	1.1
160–183 GHz	1.1	1.1

The nonlinearity of each channel was determined from the radiometric transfer functions produced from the thermal vacuum ground calibration testing [Weng *et al.*, 2013]. The nonlinearity is very well approximated by quadratic regression curves, and quadratic correction terms have been provided, based on these regressions, for optional use in the ground processing. Application of these corrections should substantially improve the overall radiometric accuracy.

Strictly speaking, for ATMS measurements, there is no direct method to evaluate radiometric accuracy on-orbit, since

**Table 2b.** Spatial Sampling (Degrees) Comparison of ATMS and AMSU/MHS

	ATMS	AMSU/MHS
23/31 GHz	1.11	3.33
50–60 GHz	1.11	3.33
89–GHz	1.11	1.11
160–183 GHz	1.11	1.11
Swath (km)	~2600	~2200

there is no known target temperature. One way to determine accuracy is to compare NWP model predicted brightness temperature (TB) with ATMS measured TB, see [Weng *et al.*, 2013] for radiance comparisons between ATMS and heritage sensors and [Weng *et al.*, 2013] for ATMS comparisons against numerical weather prediction and a radiative transfer model. Nevertheless, as illustrated in Figure 5, the on-orbit radiometric accuracy, determined by analysis from ground test measurements

(one prelaunch worst case), and using on-orbit instrument temperatures, shows large margins relative to the requirements (specified at  $<1.0$  K for channels 1, 2, and 16–22 and  $<0.75$  K for channels 3–15). This predicted accuracy performance is based on system-level ground calibration in conjunction with component-level tests and analyses. Predictions are shown in Figure 5 for both the case of using an SDR algorithm that assumes a linear transfer function and the case of applying a quadratic correction.

Regarding comparison to AMSU-A, the worst-case nonlinearity for ATMS channels 1–16, over the ground test dynamic range, was  $\pm 0.192$  K [Northrop Grumman Electronic Systems (NGES), 2012]. The corresponding AMSU-A worst-case nonlinearity, over channels 1–15, was  $\pm 0.625$  K [NGES, 2001]. In each case, nonlinearity is the dominant contribution to radiometric accuracy.

## 2.1. Response Function

The PFM receiver-level spectral response function (SRF), which includes effects of amplifier response as well as band-pass filter response, was measured for each of the ATMS channels. These band-pass characteristics were measured at  $-10^{\circ}\text{C}$ ,  $+20^{\circ}\text{C}$ , and  $+50^{\circ}\text{C}$ , at low/nominal/high DC bias levels, and with primary and secondary local oscillators.

An extensive study of the radiometric impacts of these SRFs was performed and presented by *van Delst et al.* [2010a, 2010b] and *Chidester and De Amici* [2010]. Their study evaluated the impacts of the PFM SRFs relative to ideal boxcar filters with bandwidths generally greater than the actual SRFs. To perform an impact assessment that more closely follows the actual SRFs, a comparison was made to both boxcar filters and realizable band-pass filters, using the actual measured bandwidths. The computed results indicate that the use of measured S-NPP ATMS SRFs versus the ideal SRFs has no significant impact on sensor performance. For details about these different filters and impact analysis, see *Lyu et al.* [2010].

Similar to *van Delst*, *Chidester*, and others, who use the monochromatic radiative transfer model (monoRTM) to prepare for using the Community Radiative Transfer Model (CRTM) [*van Delst et al.*, 2010a, 2010b], the monoRTM model (maintained by Atmospheric and Environmental Research, Inc.) was adopted for this study. The code and reference can be found at [http://www.rtweb.aer.com/monortm\\_frame.html](http://www.rtweb.aer.com/monortm_frame.html). These two radiative transfer models complement each other.

The measured PFM center frequencies and bandwidths were used to construct ideal boxcar (BOX), realizable perfect BP (PBP), and Gaussian (for reference only) filter SRFs. A European Centre for Medium-Range Weather Forecasts (ECMWF) training set of 83 atmospheric profiles was selected as the inputs for the monoRTM and derived the expected brightness temperatures (or radiances) were derived for the 22 S-NPP/ATMS spectral channels. The brightness temperatures were computed using measured PFM SRFs, as well as for the BOX and PBP SRFs, to determine the relative brightness temperature differences for each of the 22 ATMS channels (although only 4 representative channels are presented in this paper).

**Table 3.** Calibration Bias Offsets and Residuals

ATMS Channel	Hot Calibration Offset (K)	Hot Calibration Random (K)	Cold Calibration Offset (K)	Cold Calibration Random (K)
1	−0.060	0.078	0.398	0.172
2	−0.061	0.078	0.528	0.230
3–15	−0.058	0.078	0.220	0.138
16	−0.038	0.078	0.610	0.337
17–22	−0.036	0.078	0.114	0.108

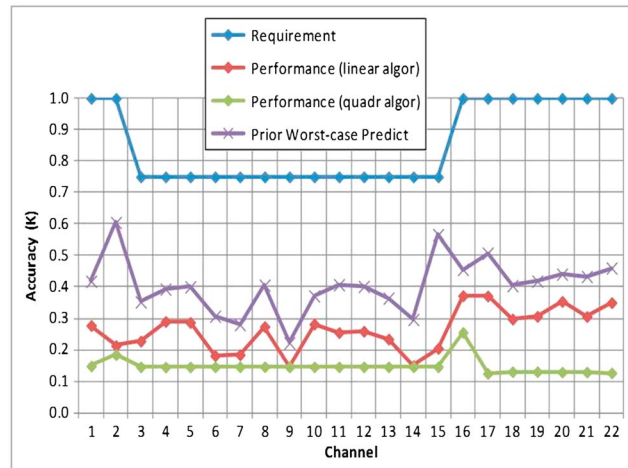


**Figure 5.** Prelaunch predicted radiometric accuracy (prior worst-case predict, in purple), and postlaunch determined radiometric accuracies (in red/green, based on linear and quadratic algorithms, respectively), using measured on-orbit parameters.

For the selected 83 profiles, the ranges of variation in temperatures and absorbing gas (six most common trace gases are adopted) amounts are compiled from the real atmosphere by *Matricardi* [2008], using the operational suite of the ECMWF forecasting system during the period of July 2006–June 2007. Thus, uncertainties from different types of profiles are expected. Among the 83 profiles, for performing radiative transfer calculations, the number of dry water vapor profiles is comparable to that of profiles covering the moister regions. The monoRTM can deal with the variations of the Planck function within a vertically inhomogeneous atmosphere. From performance studies of the fast model for simulation of Infrared Atmospheric Sounding Interferometer (IASI) and AIRS

radiances, *Matricardi* [2008] found that for scan angles from 0° to 64°, almost 98% of the channels have root-mean-square (RMS) errors  $\leq 0.1$  K.

Radiative transfer calculations were performed for a nadir-viewing observation angle, passing through atmospheric layers that are not in local thermodynamic equilibrium, and brightness temperatures were determined for the 22 ATMS channels. The polychromatic (or channel) brightness temperature,  $T_{poly}$ , was computed using the convolution of the sensor spectral response function and radiative transfer model determined brightness temperatures resulting from 83 atmospheric profiles, as follows:

$$T_{poly} = \frac{\sum_{i=1}^{i=N} (T_{mono}(i) \times SRF(i))}{\sum_{i=1}^{i=N} SRF(i)}, \quad (1)$$

where  $T_{mono}(i)$  is the monochromatic brightness temperature at frequency  $i$ , and  $SRF(i)$  is the spectral response function (normalized to 1) at frequency  $i$ .  $SRF(i)$  could be the ideal boxcar BP, perfect BP, measured PFM filter response (MFR), or measured PFM receiver-level response (MRR, which includes the effects of amplifier response functions).  $T_{poly}$ , from either BOX or PBP, was used as a gauge, subtracted from  $T_{poly}$  for either the MFR or MRR response functions, to determine deviations of brightness temperature due to the deviations of measured SRFs from the “ideal” SRFs. Namely, we define

$$\begin{aligned} \Delta T &= T_{poly}[SRF = MRR] - T_{poly}[SRF = BOX], \\ \Delta T &= T_{poly}[SRF = MRR] - T_{poly}[SRF = PBP], \\ \Delta T &= T_{poly}[SRF = MFR] - T_{poly}[SRF = BOX], \text{ or} \\ \Delta T &= T_{poly}[SRF = MFR] - T_{poly}[SRF = PBP]. \end{aligned}$$

From the model, the computed monochromatic TB for channel 1 (23.80 GHz) is relatively constant (flat), i.e.,  $\delta T_{total} = 0.015 \text{ K} \ll 269 \text{ K}$ . Therefore, equation (1) can be modified, and  $T_{mono}(i)$  can be moved outside the summation as follows:

$$T_{poly} \approx \frac{T_{mono} \times \sum_{i=1}^{i=N} (SRF(i))}{\sum_{i=1}^{i=N} SRF(i)} = T_{mono} \quad (2)$$

In this case, the shape of the channel 1 SRF has no impact on sensor performance.

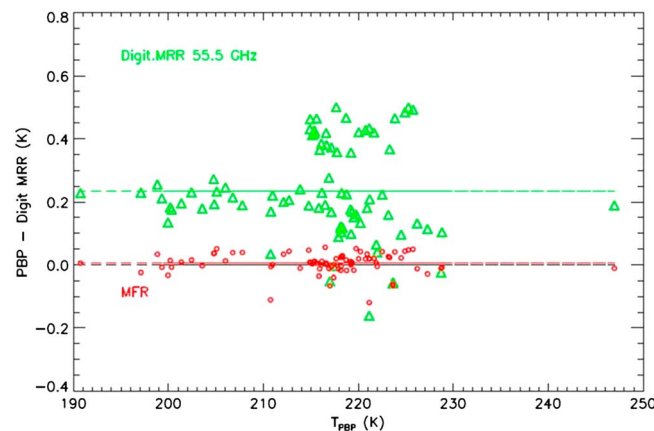


**Figure 6.** Model-derived  $\Delta T$  using PBP for S-NPP ATMS channel 9.

As explained in detail by *Lyu et al.* [2010], we use the SRFs of channel 9 as an example. The bandwidth of the measured ATMS PFM SRF is 318 MHz, which was used for the boxcar SRF. This is notably less than the 326 MHz ideal BP bandwidth adopted by *van Delst et al.* [2010b]. Our model assumptions are similar to those adopted by *van Delst et al.* [2010a, 2010b]. We could reproduce their CRTM model-predicted results. Yet with more real-life assumptions for the ideal filters, smaller predicted impacts were found to PFM sensor performance.

The  $\Delta T$ s resulting from comparison of measured receiver response to the perfect bandpasses are as follows, for four representative channels:

$$\begin{aligned}\Delta T / \text{NE}\Delta T(\text{Ch } 1) &= 0.01 \text{ K} / 0.22 \text{ K}; \\ \Delta T / \text{NE}\Delta T(\text{Ch } 6) &= 0.06 \text{ K} / 0.26 \text{ K}; \\ \Delta T / \text{NE}\Delta T(\text{Ch } 9) &= 0.20 \text{ K} / 0.26 \text{ K}; \\ \Delta T / \text{NE}\Delta T(\text{Ch } 22) &= 0.15 \text{ K} / 0.65 \text{ K}.\end{aligned}\quad (3)$$

These  $\Delta T$ s are the mean values obtained over the 83 profiles. Figure 6 presents the data for channel 9. Since the  $\Delta T$ s are all less than the corresponding channel sensitivities ( $\text{NE}\Delta T$ s), the use of actual measured SRFs versus ideal SRFs has no significant impact on the sensor performance. The boxcar BP was also found to be as good a gauge as the perfect BP filter. However, the wider boxcar BP filter, previously adopted by *van Delst* [2010b], overestimates  $\Delta T$  by about 0.1 K.

## 2.2. Power Spectral Density and Gain Correlation Measurements

During prelaunch (sensor-level or ATMS only) testing in a thermal vacuum (TVAC) chamber, ATMS underwent engineering tests to estimate the power spectral density (PSD) of each channel. The sensor-level test consisted of staring at three precision calibration targets (i.e., internal ambient target, external cold target at  $\sim 93$  K, and scene target at  $\sim 300$  K) in a continuous measurement mode that allowed estimation of the PSD. The sampling time was approximately 18 ms, which gives a maximum sampling frequency of approximately

**Table 4.** Estimated White Noise and Colored Noise Contributions to  $\text{NE}\Delta T$  (From PSD Analysis)<sup>a,b</sup>

Channel	1	2	3	4	5	6	7	8	9
Calculated $\text{NE}\Delta T^{\text{C}}$	0.27	0.35	0.41	0.30	0.29	0.29	0.28	0.28	0.31
White noise	0.25	0.29	0.33	0.24	0.24	0.26	0.23	0.24	0.27
NPS <sup>d</sup>	0.01	0.13	0.15	0.16	0.11	0.09	0.13	0.11	0.10
Channel	10	11	12	13	14	15	16	17	18
Calculated $\text{NE}\Delta T^{\text{C}}$	0.44	0.48	0.62	0.9	1.24	1.98	0.28	0.45	0.38
White noise	0.40	0.53	0.55	0.86	1.21	1.89	0.20	0.33	0.31
NPS <sup>d</sup>	0.13	0.18	0.19	0.10	0.01	0.46	0.18	0.21	0.17
Channel	19	20	21	22					
Calculated $\text{NE}\Delta T^{\text{C}}$	0.42	0.53	0.58	0.72					
White noise	0.32	0.42	0.42	0.55					
NPS <sup>d</sup>	0.24	0.21	0.25	0.32					

<sup>a</sup>All units are kelvins RMS.

<sup>b</sup>ATMS interface plate temperature of 5°C.

<sup>c</sup> $\text{NE}\Delta T$  = noise equivalent delta temperature.

<sup>d</sup>NPS = noise power stability.



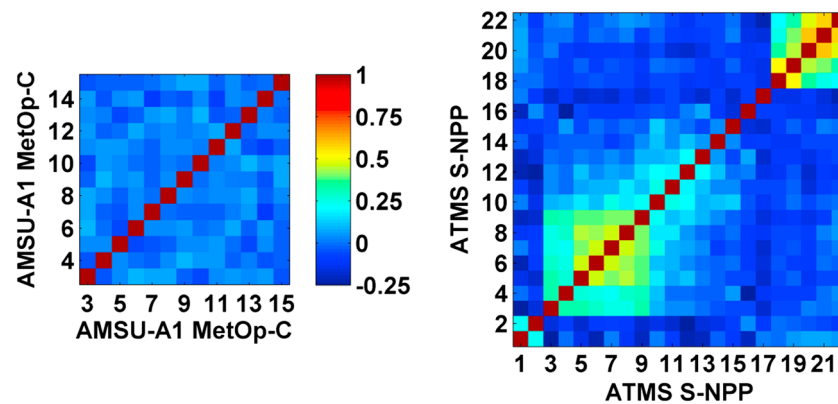


**Figure 7.** Correlation coefficients of (left) AMSU-A1 and (right) ATMS channel gains. See text for more details.

27.7 Hz to maintain spatial Nyquist conditions. Ten 12.6 s (700 samples) data sets, or segments, were collected. A 1024-point fast Fourier transform (zero padded from 700) was applied to the data. To reduce the variance of the fast Fourier transform (FFT) (i.e., the PSD estimate), the FFTs of the 10 segments were averaged. In between the segments, separate continuous measurements of the other two calibration targets allow the calculation of gain (digital numbers/K), which can be used to convert the  $\text{DN}^2/\text{Hz}$  to  $\text{K}^2/\text{Hz}$ . During satellite-level testing when ATMS is on the S-NPP satellite in a very large TVAC chamber, only two calibration targets are available. PSDs derived from sensor-level and satellite-level TVAC indicate consistent results over a variety of temperatures and over the 5.5 years between sensor-level measurements and satellite-level measurements. As expected, the PSDs showed both colored (i.e., flicker) noise and white noise, which are two primary sources of noise contributing to the NE $\Delta$ T [Hersman and Poe, 1981]. Noise power stability (NPS) is a metric that measures the contribution to NE $\Delta$ T from the colored noise. From these estimated PSDs, the contribution to NE $\Delta$ T from NPS and white noise can be estimated by calculating the flat white noise portion to the right of the “knee” in the PSD and subtracting that value from the calculated total NE $\Delta$ T (e.g., Table 1a). Another way to calculate NPS is to subtract the measured NE $\Delta$ T from the theoretical NE $\Delta$ T under stable conditions. A complete list of the estimated white noise and NPS for each channel estimated using the PSDs is given in Table 4. All ATMS receiver front end NPS requirements flowed down from the NE $\Delta$ T, and accuracy requirements were met. When compared to AMSU-A, the ATMS colored noise is higher, which is attributed to the receiver front end microwave monolithic integrated circuit (MMIC) technology in ATMS that allowed comparable NE $\Delta$ T at higher spatial sampling. The only impact noticed from the higher colored noise is the calibration striping, which is presented by Qin *et al.* [2013]. The striping artifacts are believed to arise when the periodic absolute calibration transfer function [Hersman and Poe, 1981] is unable to filter out the colored noise in the radiometric data. Filtering of the radiometric calibration data [Weng *et al.*, 2013, equation 3] can reduce the impact but has not eliminated the striping [Bormann *et al.*, 2013]. The NPS analysis presented in Table 4 presents an NPS performance metric of the complete ATMS sensor, which could be potentially used to quantify the level of calibration striping or as a diagnostic to compare against other sensors. ATMS did not have a striping requirement levied for the S-NPP satellites.

Another ATMS difference from heritage sensors is the higher gain cross-correlation between channels. The gain calculated for every scan can be made into a time series, and the gain correlation coefficients can be calculated for each channel pair. Figure 7 shows the correlation coefficients for S-NPP ATMS during satellite-level thermal vacuum testing, after integrating all instruments onto the S-NPP satellite. Figure 7 also shows the gain correlation coefficients for an AMSU-A1 unit, which has much lower gain correlation between channels. The gain was calculated using the internal calibration target at ambient temperature, and the external calibration test equipment consisting of calibration target lowered to  $\sim 90$  K. The ATMS V-band channels (3–15) share a MMIC RF low-noise amplifier (LNA). Furthermore, ATMS channels 3–9 share a mixer and IF amplifiers, channels 10–15 share their own mixer and IF amplifiers, and channels 12–15 use surface acoustic wave filters. AMSU-A1 has completely separate (i.e., independent) receiver front ends for channels 3 through 8 and 15. AMSU-A1 channels 9 through 14 share a mixer and amplifiers but no RF LNA. Combining the receiver front ends helped reduce the size, weight, and power consumption of ATMS over heritage

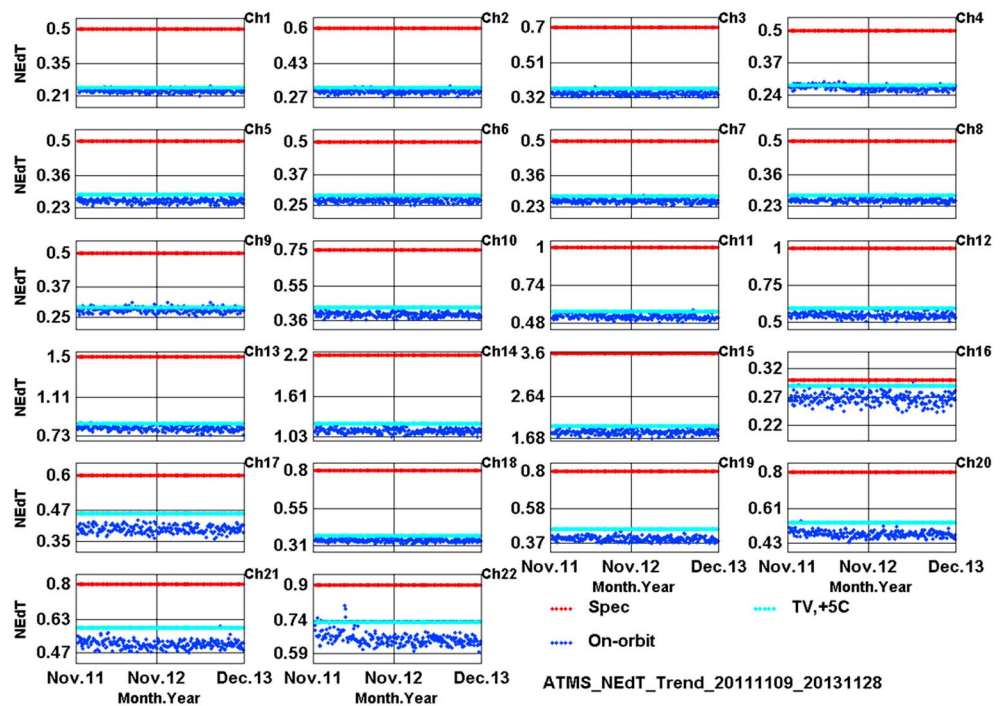


**Figure 8.** Radiometric sensitivity over 2 years, channels 1–22. “Spec” (red line) is the NEΔT requirement for each channel, “on-orbit” (dark blue) is the computed NEΔT after S-NPP launch, and “TV,+5C” (light blue) is the prelaunch measured NEΔT with the cold plate temperature at +5°C. Gain stability is manifested in both NEΔT and NEΔT stability. This figure shows quantitatively that for ATMS 2 year on-orbit performance, there has been virtually no change in NEΔT after launch, and NEΔT specifications are being met for all channels, and significantly exceeded for most channels for the first 2 years of on-orbit performance.

sensors (see section 2). The correlation coefficients reported in this paper complement the findings by [Bormann *et al.*, 2013, Figure 6], and the coefficients presented in Figure 7 are independent of a NWP model or atmospheric variability. It is assumed that the correlation in the calibrated data [Bormann *et al.*, 2013, Figure 6] is due to the correlated gain shown in Figure 7, which is due to the flicker noise that is not removed by calibration (i.e., calibration striping).

### 3. On-Orbit Performance Assessment

All ATMS functionality and engineering telemetry are nominal and fully consistent with ground test data. The sections below present summary results from assessments of on-orbit data, obtained during the S-NPP calibration/validation phase.

#### 3.1. Instrument Thermal Stability

The critical performance parameters for which stability was assessed were the receiver shelf temperatures, the gain of each channel, and the warm calibration load temperatures. By orbit 164, it was determined that all these parameters were sufficiently stable to meet radiometric performance requirements, but there was still a noticeable warm-up drift. A reassessment on orbit 182 indicated no noticeable drift, and these data can be used to assess magnitudes of systematic orbital variations.

The observed stabilities for all channels were significantly better than had been assumed in the analyses for predicting radiometric calibration accuracy. For example, the channel 3 gain stability is  $1 \times 10^{-5}$  dB/s versus a predicted  $8 \times 10^{-5}$  dB/s, and the warm load stability is  $<0.00035$  K/s versus a predicted 0.001 K/s. Consequently, the calibration accuracy assessment in section 2 and in Figure 5, based on these observed stabilities, shows some improvement over the previous predictions. Subsequent telemetry, collected over a full year, indicates that the orbital variations for orbit 182 are a seasonal worst case. The minimum orbital variations are less than half of these worst-case values.

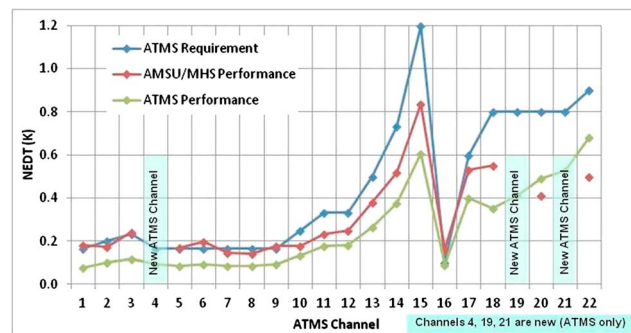


**Figure 9.** Sensitivity of ATMS channels, for orbit 182, scaled to a 300 K scene and converted to AMSU equivalent footprints (i.e., ATMS requirements and performance, for channels 1–16, are divided by 3 to account for a factor of 9 shorter sampling intervals).

### 3.2. Radiometric Sensitivity

The sensitivities of all channels were derived from warm load counts data, by computing the standard deviation of counts relative to a linear regression, and using an average gain value to convert to NE $\Delta$ T. Note that NE $\Delta$ T is defined as the standard deviation of the radiometer output temperature in kelvins when the antenna views a 300 K uniform and stable target. For the on-orbit performance evaluation, since we do not have observations at a given constant temperature or at 300 K, we could use only the warm and/or cold target data to implement

this study. Before computing NE $\Delta$ T, we first needed to remove scan-to-scan gain fluctuations and diurnal and/or orbital variation effects in the data. The 2 year trending of on-orbit NE $\Delta$ T is extrapolated to a scene temperature of 300 K to compare with the ATMS requirements. Trending results are shown in the charts in Figure 8. This figure also shows the NE $\Delta$ Ts computed from the (prelaunch) ground calibration test data, demonstrating that there has been virtually no change in NE $\Delta$ T after launch, and NE $\Delta$ T specifications are being met for all channels, and significantly exceeded for most channels for the first 2 years on-orbit performance. Thus, the radiometric stability is very good.

In Figure 9, both the ATMS data-derived NE $\Delta$ Ts and the ATMS requirements for channels 1–16 have been divided by three, to allow a direct comparison with AMSU-A. This is because the data sampling interval is a factor of 3 smaller for ATMS, in both the along-track and cross-track directions, for a total factor of 9. When ATMS data is averaged to the equivalent AMSU footprint, as is done for fusion with CrIS data, there is thus a factor of the  $\sqrt{9}$  ( $=3$ ) reduction of noise in the final resampled SDR [CrIS EDR ATBD; Appendix D2]. This adjustment for spatial resolution was not done for channels 17–22, since they are compared against the MHS, which has the same sampling and scanning rate as the ATMS. This data demonstrates significant improvements in sensitivity, as would be expected from the more advanced receiver front-end technology.

### 3.3. Space View Selection

After initial functionality testing, ATMS SDR team members, made up of members from NASA, NOAA/Center for Satellite Applications and Research, Massachusetts Institute of Technology Lincoln Laboratory, Northrup Grumman Electronic Systems (NGES), Northrup Grumman Aerospace Systems (NGAS), Naval Research Laboratory, Raytheon, and Space Dynamics Laboratory (SDL), selected an ATMS Scan Profile (SP) using a procedure similar to the MHS procedure. ATMS has four Space View Sectors (SVSs), the operational SVS is the one with the least amount of interference from the S-NPP spacecraft and/or Earth intercepting its antenna sidelobes. The four SVSs, corresponding to ATMS four scan profiles, are centered at view angles 6.66°, 8.33°, 10.0°, and 13.33° below S-NPP + Y axis. Each SVS (or SP) consists of 4 different SV pixels 97–100, hereafter called SV1, SV2, SV3, and SV4, respectively. The scan pixel 97 (or SV1) is closer to the Earth limb, and the scan pixel 100 (or SV4) is closer to the S-NPP satellite platform.

To implement the SP selection, we examined contiguous time series data at different SPs. After ATMS activation and checkout, at least 48 h of data was collected at each SP (starting at SP1 and repeating SP1 after completing SP4). The second SP1 data included some lunar contaminated data, which were discarded.

Two analyses of the SP data are presented here. One analysis shows the correlation of the various SPs and the upwelling Earth radiance. The other analysis compares the statistics of the first and last SVS pixel for each SVS. The two analyses determined that SVS 1 (centered at 6.66° off the antisunside horizon, i.e., closest to the spacecraft) should be the operational SVS. The correlation between each SVS's radiometric counts and the upwelling radiance indicates that all SVS had some channels with contamination. The SV differencing method showed that SP1 was most uniform between SV1 and SV4. Another deciding factor was that only

**Table 5.** Correlations of the SVS (i.e., SP) Versus the Nadir Upwelling Radiation

Channel	1	2	3	4	5	6	7	8	9	10	11
SP1 (6.66°)	0.569	0.379	0.167	0.174	0.196	0.128	0.051	0.023	0.034	0.008	0.058
SP2 (8.33°)	0.578	0.408	0.176	0.175	0.196	0.108	0.029	0.017	0.026	−0.002	0.068
SP3 (10.0°)	0.584	0.433	0.198	0.206	0.234	0.104	−0.072	−0.110	−0.060	−0.016	0.057
SP4 (13.33°)	0.571	0.391	0.168	0.179	0.202	0.084	−0.073	−0.099	−0.008	−0.055	0.038
Channel	12	13	14	15	16	17	18	19	20	21	22
SP1	0.223	0.207	0.161	0.063	0.485	0.095	−0.006	0.012	0.027	0.007	−0.016
SP2	0.233	0.226	0.171	0.064	0.457	0.050	−0.034	−0.017	−0.014	−0.026	−0.040
SP3	0.228	0.217	0.168	0.060	0.466	0.008	−0.005	−0.011	0.024	0.016	0.006
SP4	0.221	0.221	0.168	0.057	0.506	−0.006	−0.014	0.031	0.015	0.004	−0.005

SP1's antenna patterns were measured prelaunch and incorporated into the calculation of the cold space bias correction [Weng *et al.*, 2013, paragraph 15].

Some of the ATMS channels had all four SVS correlated with their Earth View Sector (EVS) measurements. It is expected that the SVS will see some of the Earth's limb and the calibration algorithm accounts for this with a cold space bias correction, which was derived from the SVS (SP1) pre-launch antenna pattern measurements. The cold space bias correction accounts for Earth and spacecraft contamination into the antenna sidelobes, but the ATMS SDR algorithm bias correction is not a function of the nadir upwelling brightness temperature. Scatter plots of the nadir beam position brightness temperature versus the radiometric counts of the first beam position of the SVS (closest to the Earth's limb) did not show significant differences among the four SPs or SVSs. Note that the SVS counts were used to calibrate the nadir brightness temperature (or more exactly, the antenna temperature). The strongest correlations (0.4–0.5) were seen in the 23.8, 31.4, and 89 GHz channels, which were also the quasi-vertical and window channels. The calculated correlations can be found in Table 5. The lower V-band channels also had some correlation but at 0.2. The nadir cross correlation analysis does not show us an optimized SVS, because choosing a SVS closer to

**Table 6.** Comparisons of SV1–SV4 for SP 1–4

Channel	SP1	SP2	SP3	SP4	SP1
	(18 Nov 2013) SV1–SV4 <sup>a</sup>	(26 Nov 2013) SV1–SV4	(29 Nov 2013) SV1–SV4	(1 Dec 2013) SV1–SV4	(8 Dec 2013) SV1–SV4
1	<b>0.772<sup>b</sup></b>	0.812	2.675	4.194	<b>0.727</b>
2	<b>−1.412</b>	0.125	3.186	0.841	<b>−1.333</b>
3	<b>−0.255</b>	0.789	1.566	3.803	<b>−0.322</b>
4	<b>−0.001</b>	0.765	1.666	2.824	<b>−0.021</b>
5	<b>−0.131</b>	0.754	1.368	3.266	<b>−0.193</b>
6	<b>−0.035</b>	1.182	1.850	2.913	<b>−0.032</b>
7	<b>0.457</b>	0.533	1.028	2.211	<b>0.463</b>
8	<b>0.309</b>	0.648	1.191	2.324	<b>0.326</b>
9	<b>0.366</b>	0.711	0.995	2.298	<b>0.303</b>
10	<b>0.231</b>	0.580	1.109	1.583	<b>0.311</b>
11	<b>0.403</b>	0.845	0.665	1.540	<b>0.271</b>
12	<b>0.487</b>	0.751	0.821	2.219	<b>0.567</b>
13	<b>0.191</b>	0.432	1.389	1.879	<b>0.210</b>
14	<b>0.120</b>	0.547	1.788	2.111	<b>0.186</b>
15	0.690	0.182	1.762	2.289	<b>−0.121</b>
16	<b>1.185</b>	2.039	2.848	2.769	<b>1.142</b>
17	0.728	0.935	<b>0.360</b>	1.021	0.715
18	<b>0.401</b>	0.546	0.555	0.485	<b>0.365</b>
19	<b>0.475</b>	0.553	0.481	0.539	<b>0.398</b>
20	<b>0.580</b>	0.755	0.685	0.587	<b>0.560</b>
21	<b>0.472</b>	0.609	0.586	0.489	0.532
22	<b>0.402</b>	0.635	0.639	0.593	<b>0.454</b>

<sup>a</sup>SV1 is closer to the Earth's limb, and SV4 is closer to the S-NPP satellite platform; SP1 is closer to the S-NPP spacecraft platform, and SP4 is closer to the Earth's limb.

<sup>b</sup>Bold values mean the lowest SV1–SV4 among the four different SPs.

the spacecraft and therefore farther from the Earth's limb did not reduce the correlation. As a reality check, a spectral analysis was completed on the EVS, SVS, and internal calibration target (ICT) time series, and the EVS harmonics were seen in the SVS spectrum but not in the ICT spectrum.

Another approach is to analyze count statistics of SV1 and SV4 among the different SPs. The SP with the lowest mean counts for the largest number of ATMS channels would be the selected SP. The low-frequency noise components resulting from diurnal variation and/or orbital variation in the data needed to be removed first. From the count statistics of SV1 and SV4, however, we find that the scan-to-scan gain fluctuations among four different SPs make the count statistics of SV1 and SV4 results inconclusive about which SP would be best. Moreover, for the repeatability tests of SV1 and SV4 at the same SP1, we did not obtain consistent statistics between data collections. Consequently, we need to find another approach in which the count statistics would be free of the impact from the scan-to-scan gain fluctuations.

A slightly modified approach was used that studied the count statistics of the differences between SV1 and SV4 (i.e., SV1–SV4). After removing the scan-to-scan gain fluctuations from each SP, we found consistent count statistics. In addition to the scan-to-scan gain fluctuations in the SV data, we need to remove the diurnal and half orbital low-frequency components in the data. The low-frequency noise components have been identified through power spectrum analysis (i.e., FFT).

The improved methodology provided the count statistics for SPs 1–4 in Table 6. SV4 is the closest measurement to the S-NPP spacecraft platform, and SV1 is closer to the Earth's limb, which is 200–300 K hotter than the cold space scene. Since both SV1 and SV4 view the same cold space almost at the same instant, separated by 54 ms, if there were no interference from the surroundings, then the measured counts would be comparable to each other. As shown in Table 1b, when the measured SV1 counts are larger than the SV4 counts, it means that the impact from ATMS antenna sidelobes interacting with the Earth's limb is larger than that from interaction with the S-NPP platform. This implies that the best SVS has the smallest SV1–SV4 difference for the highest number of ATMS channels, which is SP1.

### 3.4. Maneuvers

Large-angle spacecraft maneuvers are an invaluable tool for evaluating on-orbit scan-dependent biases and sidelobe characteristics. On past satellites with operational sounders, this was rarely permitted for risk reasons and then only at the end-of-life [Kleespies *et al.*, 2007b]. Fortunately, on S-NPP, maneuvers were permitted during commissioning for instrument calibration purposes. These maneuvers also provided invaluable data for analyzing striping [Qin *et al.*, 2013]:

1. 9 December 2011: Roll 65° antisunside and Roll 25° sunside.
2. 12 January 2012: Roll 65° antisunside and Roll 25° sunside.
3. 20 February 2012: Pitch 360°.

The goal of the ATMS pitch maneuver was to establish the baseline radiometer output (counts) by viewing a uniform scene (cold space). In this maneuver, the S-NPP spacecraft was pitched to enable ATMS to acquire full scans of deep space, providing a uniform field of view, and thus allowing any scan bias, to be characterized. When the Earth's disk lies totally outside the ATMS beams and their larger sidelobes, there can be good sensitivity to any anomalies introduced by obstacles near the spacecraft itself. Therefore, the pitch maneuver data were analyzed for information about fore and aft sidelobe levels. Similarly, the ATMS roll maneuver data are analyzed for information about the left and right sidelobe levels. Due to space limitations, we have omitted these sidelobe results.

### 3.5. Scan-Dependent Bias

One of the phenomena that have long been observed for cross-track scanning radiometers (e.g., AMSU-A) is a radiometric brightness temperature offset that is a systematic function of scan angle, with significant asymmetry. Based on extensive analyses of scene data by various ATMS SDR team members, attempts have been made to empirically model this scan-dependent bias and to apply a correction. Although several hypotheses have been considered, the root cause had never been established. Initial analysis indicates that ATMS has a smaller scan bias asymmetry than heritage radiometers [Bormann *et al.*, 2013]. During the S-NPP ATMS calibration/validation phase, pitch-over maneuvers were performed, which allowed a view of cold space across the entire scan, with virtually no sidelobe intercepts with the Earth. This provided valuable



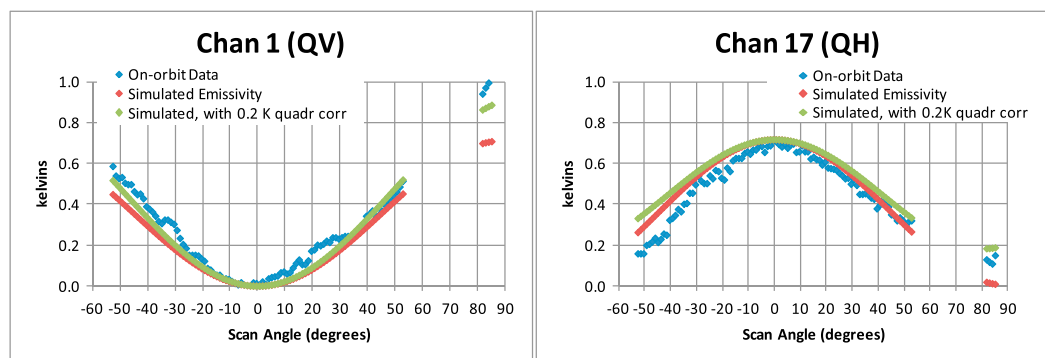


**Figure 10.** Scan-dependent bias, obtained from calibration/validation pitch maneuver, compared to simulated effect of reflector emissivity.

unpolarized data from a uniform source to permit a better characterization of this potential scan-dependent bias phenomenon and for investigating candidate causes. Figure 10 shows examples of this scan bias, obtained from the pitch maneuver on 20 February 2012. Scan angles from  $-52.725^\circ$  to  $+52.725^\circ$  are in the Earth View Sector, and the 4 samples at  $81.675^\circ$ – $85.005^\circ$  are in the Space View Sector. Counts were converted to brightness temperatures using the average gain of each channel and applying offsets such that (1) each QV channel temperature at  $0^\circ$  scan angle is at 0 K, and (2) each QH channel temperature at  $0^\circ$  scan angle is equal to twice the temperature at  $+45^\circ$ . These offsets are not intended to produce absolute actual sky temperatures but rather to facilitate relative comparisons of the bias effect.

It is quite significant that when observing the virtually uniform cosmic background, there is a highly symmetrical variation with scan angle: for the QV channels, it is a good fit to a cosine-square curve, and for the QH channels, it is a good fit to a sine-square curve. See Table 1b for identification of QV and QH channels. For both QV and QH channels, the polarization in the local Earth frame rotates during the scan. This is due to the fact that the scanning is implemented by a cross-track scanning reflector that is illuminated by a fixed feed horn [Leslie *et al.*, 2013].

### 3.5.1. Flat Reflector Emissivity

The likely explanation for these observations is that the rotating scanning assembly of the ATMS is introducing a polarized contribution to the received signal, due to reflector emissivity. The flat-plate scanning reflector is a beryllium plate with a thin layer of nickel and an outer layer of  $0.6\ \mu\text{m}$  gold plating. It is well known that reflectors composed of a thin conductive layer can present much higher microwave emissivity than the theoretical values for bulk materials [Kerr *et al.*, 2009; Teverovsky, 2003]. For example, the estimated emissivity for the Special Sensor Microwave Image Sounder (SSMIS) vapor-deposited aluminum layer, at 50 GHz, is on the order of 0.25% [Kunkee *et al.*, 2008] versus the Hagen-Rubens theoretical value of 0.08% for bulk aluminum. This is likely due to the irregularities and granularity of the conductive layer. When viewed at a  $45^\circ$  incidence angle, as is the case for the ATMS configuration, this emissivity is polarized. As an example, if the emissivity were 0.37%, and for a physical temperature of  $0^\circ\text{C}$ , the resulting QV and QH contributions from the reflector emissivity would be as shown in the red curves of Figure 10. This is very near to the observed on-orbit biases, except that the on-orbit data shows a greater increase at large scan angles, especially at the cold calibration angles ( $81.7^\circ$ – $85.0^\circ$ ). No actual measurements have been made of the ATMS reflector emissivity, but experience from other satellite radiometers indicates that the value hypothesized above is certainly plausible. For example, the original design of the SSMIS reflector (vapor-deposited Al on graphite epoxy) had about 1.0% emissivity. The UARS (Upper Atmosphere Research Satellite) Microwave Limb Sounder's primary reflector (vapor-deposited Al on graphite/cyanate composites) had comparable measured emissivities at 63 GHz and 183 GHz [Jarnot *et al.*, 1996] against a silver plate standard.

The data indicate that there is a secondary factor that increases symmetrically with scan angle, regardless of polarization. This contribution was modeled as a quadratic function of scan angle, with 0.2 K brightness temperature at  $90^\circ$ . The result of adding this to the reflector emissivity effect, as shown in Figure 10, is that the QV channels will have a somewhat greater magnitude of variation than the QH channels, and a notable increase at the cold calibration angles, which fits well with the on-orbit data. The physical cause of this

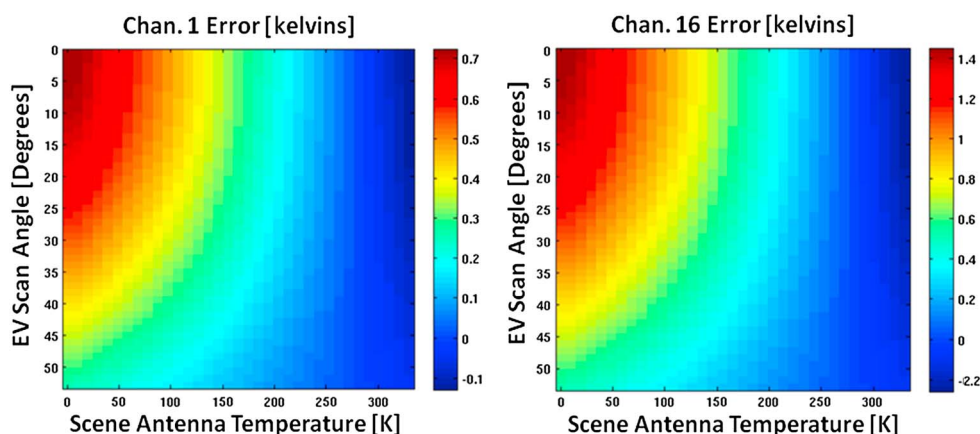


**Figure 11.** Simulated error per scene temperature and scan angle for (left) channel 1 and (right) channel 16.

secondary contribution has not yet been established but may be due to antenna radiation spillover within the instrument and/or Earth sidelobe intercepts.

Another minor contribution is due to antenna sidelobe intercepts with the spacecraft, which occurs on the sunside (i.e., negative scan angles), thus producing an asymmetric deviation from the sine-square and cosine-square functions. As seen in Figure 10, channel 1 has higher temperatures on the sunside (negative scan angles) than on the cold side. The same effect is seen for channels 2–15. For channels 16–22, the sunside has lower temperatures. This is likely because the antenna aperture for channels 1–15 has a clear view to the horizon, with some intercept of the solar array. Channels 16–22, on the other hand, are obstructed by the Clouds and the Earth's Radiant Energy System instrument, which may be reflecting radiation from cold space in the zenith direction. The observed asymmetric contributions are no more than about 0.2 K, which is consistent with the predicted worst-case spacecraft intercept contributions of up to 0.4 K.

### 3.5.2. Correction Algorithm

According to this proposed model for the scan-dependent bias, the magnitude of the effect will be proportional to reflector physical temperature. There will also be a scan-dependent reduction of reflectivity, introducing another error source, proportional to the scene brightness temperature. This means that a correction algorithm, to be applied operationally to scene data, needs to account for these additional factors. The flat reflector emissivity would introduce the worst bias for a cosmic background scene (i.e., when the scene brightness temperature is farthest from the reflector's physical temperature). The scan bias error introduced by the flat reflector emissivity across the full scene brightness temperature range was bounded using a simple sensor system model. Three separate models were used in the sensor system model: (1) the flat reflector corruption, (2) the antenna temperature to digital counts, and finally, (3) the calibration algorithm (counts to antenna temperature). Using the simple models, the results are in Figure 11. The cosmic background scene from the pitch over maneuver matched the modeled error. Based on an orbit's worth of ATMS data, the channel's median brightness temperature gives an error of  $\sim 0.4$  K at nadir for the quasi-vertical polarized channels if the antenna temperatures are not corrected. While the error is much smaller for the quasi-horizontal channels ( $\sim 0.1$  K, not shown). It should also be noted that any correction used in the SDR algorithm should apply appropriate corrections to the warm and cold calibration views as well as to the scene viewing sector. The emissivity correction would be applied to the ATMS TDR data product as the emissivity impacts the antenna temperature.

### 3.5.3. Empirically Derived Emissivity Values From Pitch Over Maneuver

The ATMS pitch over maneuver data was used to derive the emissivity values for each channel by using the emissivity correction algorithm and free parameters. The emissivity correction needs two parameters, which are the normal incident emissivity and the reflector's physical temperature. The reflector's temperature comes from ATMS telemetry, in particular, a temperature sensor on the ATMS scan drive attached to the rotating flat reflectors. Through simple sensitivity analysis, it was determined that the error in the physical temperature produced a minimal impact compared to the normal emissivity. Each channel's emissivity was derived by increasing the normal emissivity in the corrected calibration algorithm from 0 to 1% emissivity in

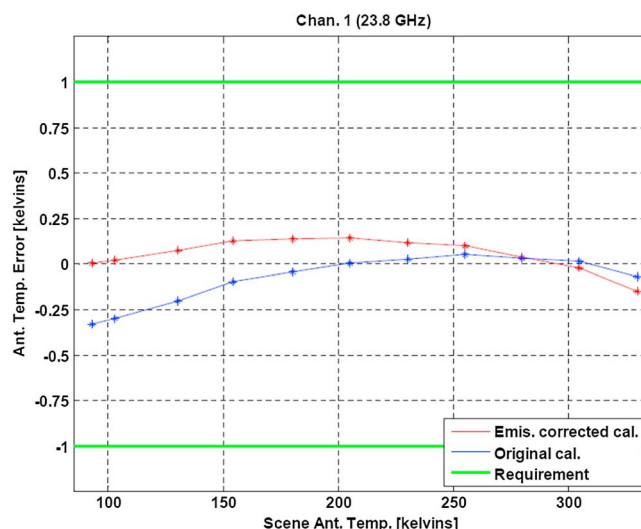


**Figure 12.** S-NPP/ATMS data (channel 1 at 23.8 GHz) from sensor-level TVAC testing. The testing involved two external targets. One is the SVS at 93 K and another in a subset of the EVS (scene). Internal target was at 283 K.

However, the gold plating layer thickness ( $0.6 \mu\text{m}$ ) is comparable to the skin depth at the lower frequency channels:  $0.51 \mu\text{m}$  at 23.8 GHz (channel 1) and  $0.33 \mu\text{m}$  at 57.3 GHz. The resulting increased penetration into the underlying Ni layer at 23.8 GHz is the likely explanation for the higher emissivity of channel 1 compared to the 50 GHz channels. The data at  $\sim 83^\circ$  is the SVS measurements used in the calibration. The difference in brightness temperature between SVS and EVS are under investigation, but theories were presented earlier. In the next section, the derived emissivity was then used in the sensor-level TVAC analysis to see the impact on absolute calibration accuracy.

### 3.5.4. Verification

The empirically derived emissivity values per channel were then used to correct the calibration of the data during the sensor-level TVAC testing. Figure 12 gives the ATMS calibration accuracy for channel 1 (23.8 GHz) with and without the emissivity correction (using the empirically derived emissivity and the scan drive temperature sensor measurements). We would expect that calibration accuracy at the two calibration points to be close to zero (at 93 and 283 K). The original, uncorrected curve has an offset at 93 K, which was previously unexplained. The red curve (using the correction) eliminates this discrepancy, thus helping to validate the scan-dependent emissivity model. The derived emissivity values will have to be verified by some combination of theory, simulation, or measurement. NGES is currently trying to quantify the emissivity in the laboratory.

### 3.6. Lunar Intrusion Mitigation

For one lunar intrusion (LI) case, on 5 December 2011, at 6:41 UT, using SP1 at this date/time, all 4 SV pixels were contaminated for the K/Ka bands, and only 1 SV pixel was free of lunar contamination for V, W, and G bands. These results are consistent with those depicted in Figure 13, when the lunar phase is  $-57.48^\circ$  and the moon's center is  $\approx 0.15^\circ$  below SV2 FOV center. If we adopt the original plan to not perform SDR/TDR processing when there are fewer than 3 contamination-free SV pixels, then at 6:41 UT, we would lose about 25 min of data for K/Ka bands (channels 1 and 2) data and 7–12 min worth of data for all other bands (even though there was one good SV for those bands). Then from 3 December to 5 December 2011, we would lose, at most, about 10 h worth of TDR, calibrated SDR, remap SDR, and EDR data products during these times/dates.

The operational algorithm document (OAD) for the ATMS SDR provides the original lunar intrusion mitigation algorithm: The counts from the cold calibration views are averaged over  $N_{\text{cc}} (=10)$  scans. Within each scan, at least three “good” cold target samples are present. Otherwise, that scan is excluded in the count averaging. If the weighted sum of all scans not flagged as “bad” falls below a specified percentage—90% of the total

increments of 0.05%. The derived emissivity was selected by finding the minimum standard deviation of the brightness temperature across the Earth View Sector ( $\pm 52^\circ$ ). Typical results for S-NPP/ATMS pitch over maneuver data with several values of normal emissivity in the emissivity-corrected calibration algorithm can be found in previous work [Leslie et al., 2013]. For channel 1, the result was 0.4%, while the 50 GHz channels were 0.2% which matches the SSMIS-derived results at 50 GHz of 0.25% [Kunkee et al., 2008]. According to the Hagen-Rubens theory for a perfectly smooth surface bulk conductor, the emissivity should be proportional to the square root of frequency. Also, the degradation due to surface roughness and granularity should increase with frequency.

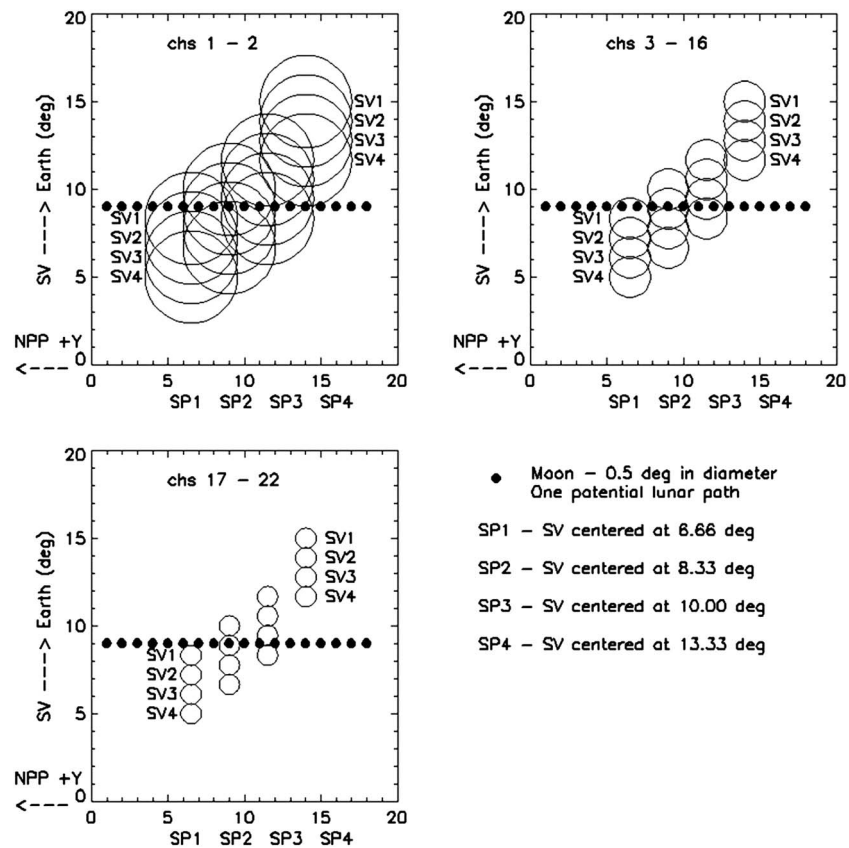


**Figure 13.** ATMS SV sector (or SP) design. SV4 is closer to S-NPP + Y, corresponding to S-NPP platform; SV1 is closer to the Earth's limb.

weight for cold count averaging—it is deemed not possible to reliably determine the averaged cold count of this channel for the current calibration cycle. This channel is then flagged by turning the data sufficiency flag on. Failing the data sufficiency test results in an unsuccessful calibration cycle for that channel. The brightness temperatures and corrected brightness temperatures are then filled with fill value  $-999.5$  K. Future versions of the OAD will include a correction for the contaminated SV counts to yield a LI-corrected scene brightness temperature instead of a fill value. The current plan for this LI-implemented LI correction algorithm is described as follows.

Pixels that are corrupted by the moon are ignored and replaced with the previous unaffected SV data. Namely, when encountering LI, if the LI-induced temperature of each SV pixel jumps by  $0.2$  K or more in the processing scan, the ATMS operational code adopts good SV data from a previous scan (even 1 SV pixel or the average of all good SVs, if applicable) to substitute for the contaminated SV in the current scan. This LI mitigation algorithm, developed by NGAS members of the ATMS SDR team, was accepted by the S-NPP ATMS SDR team on 4 December 2013 and is implemented in the ATMS SDR code. Note also that when any one of the 4 SV pixels is LI-contaminated for the processing scan, the LI flag will be turned on. This updated LI correction algorithm has been verified to be quite effective and with errors within  $0.1$  K in the worst case when all SV pixels are contaminated.

It appears to be possible to remove even this additional  $0.1$  K error resulting from manually inserting previous good SV data, by switching between different SPs as demonstrated in Figure 13. Specifically, we can predict lunar intrusion relative to each SV position in the SP1, and we can switch to SP4 during those lunar contamination periods. For these worst lunar contamination cases (e.g., 5 December 2011), we will obtain at least 3 (out of 4) SV pixels per calibration scan. Moreover, during the optimal SP selection test, we operated in each SP data for at least 5 days. And our studies indicated that the SV count levels and statistics of SPs 1–4 are comparable to each other. The only differences among different SPs are due to differences in gain. Most

importantly, this new mitigation method of switching between different SPs would maintain optimal data quality. Evaluation of this switching method is continuing.

## 4. Conclusion

In this paper, we have presented results from on-orbit evaluations of ATMS instrument thermal stability, radiometric sensitivity, accuracy, and scan-dependent bias. We have also described the calibration maneuvers, the lunar intrusion detection/mitigation approach, and the selection of the space view scan profile. These evaluations from the initial 2 years of operation of the S-NPP ATMS, indicate that this first flight unit of the newest operational microwave sounder series is performing well, meeting its requirements while improving on the capabilities of heritage sounders. The evaluations described in this paper contributed to the ATMS SDR product reaching “provisional” maturity status in December 2013.

Current and near future work includes improving the scan bias and beam efficiency corrections.

A nearly identical follow-on flight unit is presently in testing, for eventual deployment on the JPSS-1 spacecraft. The performance results from that unit will help us to unravel some of the remaining issues for S-NPP ATMS, e.g., emissivity versus scan angle, and the performance evaluation results presented in this work (for S-NPP) have provided valuable insight regarding testing of all subsequent flight units in the ATMS series.

## Acknowledgments

The authors wish to acknowledge the efforts of many colleagues from JPSS, S-NPP, Northrop Grumman, Ball Aerospace, and NPOESS over more than a decade that made the successful ATMS launch and operations possible. We would like to thank Vivienne Payne and the monoRTM team for their valuable technical assistance. And we wish to thank C. Lynn Chidester (USU/SDL), Giovanni De Amici (NGAS, now GSFC), and Mike Landrum (NGES) for their dedication to provide accurate spectral response function data for use by the NWP community. Operational data used in this paper are available free through NOAA data archives. Some test data are archived separately. Inquiries regarding the latter should be directed to the authors.

## References

- Aumann, H., et al. (2003), AIRS/AMSU/HSB on the Aqua mission: Design, science objectives, data products, and processing systems, *IEEE Trans. Geosci. Remote Sens.*, 41(2), 253–264.
- Bormann, N., A. Fouilloux, and W. Bell (2013), Evaluation and assimilation of ATMS data in the ECMWF system, *J. Geophys. Res. Atmos.*, 118, 12,970–12,980, doi:10.1002/2013JD020325.
- Cardinali, C. (2009), Monitoring observation impact on short-range forecast, *Q. J. R. Meteorol. Soc.*, 135, 239–250.
- Chidester, L., and G. De Amici (2010), ATMS-DigitizeData\_Giovanni\_Chidester30Aug10.xlsx, digital data, compiled by L. Chidester.
- Hersman, M. S., and G. A. Poe (1981), Sensitivity of the total power radiometer with periodic absolute calibration, *IEEE Trans. Microwave Theory Tech.*, MTT-29(1).
- Jarnot, R. F., R. E. Cofield, J. W. Waters, D. A. Flower, and G. E. Peckham (1996), Calibration of the Microwave Limb Sounder on the Upper Atmosphere Research Satellite, *J. Geophys. Res.*, 101(D6), 9957–9982.
- Joint Polar Satellite System Algorithm Theoretical Basis Document Cross-Track Infrared Sounder Environmental Data Record (2010), 474-00056, A.
- Kerr, A. R., et al. (2009), Loss of Gold Plated Waveguides at 210–280 GHz, Atacama Large Millimeter/Submillimeter Array Memo #585.
- Kleespies, T. J. (2007a), Relative information content of ATMS and the combination of AMSU and MHS, *IEEE Trans. Geosci. Remote Sens.*, 45(7), 2224–2227.
- Kleespies, T. J., R. Smith-Dearring, J. Woodward, J. Shepherd, C. Gliniak, W. Chadwick, J. Walters, and D. Han (2007b), Evaluation of scan asymmetry in the NOAA-14 Microwave Sounding Unit by a pitch maneuver, *IEEE Geosci. Remote Sens. Lett.*, 4(4), 621–623, doi:10.1109/LGRS.2007.903394.
- Kunkee, D. B., S. D. Swadley, G. A. Poe, Y. Hong, and M. F. Werner (2008), Special Sensor Microwave Imager Sounder (SSMIS) radiometric calibration anomalies—Part I: Identification and characterization, *IEEE Trans. Geosci. Remote Sens.*, 46(4), 1017–1033, doi:10.1109/TGRS.2008.917213.
- Leslie, R. V., et al. (2013), S-NPP ATMS: Reflector Emissivity Model, Mitigation, & Verification, International Geoscience and Remote Sensing Symposium, 2013 IGARSS Proceedings.
- Lyu, J. C.-H., et al. (2010), JPSS/NPP/ATMS Sensor Performance Related Study – PFM Filter Spectral Response Data & Impact, paper presented at NASA Sounder Science Team Meeting, Greenbelt, MD.
- Matricardi, M. (2008), The Generation of RTTOV Regression Coefficients for IASI and AIRS Using a New Profile Training Set and a New Line-By-Line Database, ECMWF Technical Memorandum No. 564. [Available at [http://www.ecmwf.int/publications/library/ecpublications/\\_pdf/tm/501-600/tm564.pdf](http://www.ecmwf.int/publications/library/ecpublications/_pdf/tm/501-600/tm564.pdf), which has details on the 83 atmosphere profiles dataset.]
- Muth, C., W. A. Webb, W. Atwood, and P. Lee (2005), Advanced Technology Microwave Sounder on the National Polar-Orbiting Operational Environmental Satellite System, Int’l Geoscience and Remote Sensing Symposium, 2005 IGARSS Proceedings, 1, doi:10.1109/IGARSS.2005.1526113.
- Northrop Grumman Electronic Systems (NGES) (2001), AMSU-A-1 Calibration Log Book, S/N 105, Report 11322A.
- Northrop Grumman Electronic Systems (NGES) (2012), ATMS Calibration Data Book, ATMS PFM, Report 14029C.
- Poe, G. (1990), Optimum interpolation of imaging microwave radiometer data, *IEEE Trans. Geosci. Remote Sens.*, 28(5), 800–810.
- Qin, Z., X. Zou, and F. Weng (2013), Analysis of ATMS striping noise from its Earth scene observations, *J. Geophys. Res. Atmos.*, 118, 13,214–13,229, doi:10.1002/2013JD020399.
- Teverovsky, A. (2003), Introducing a New Member to the Family: Gold Whiskers, NASA GSFC Internal Memo.
- van Delst, P., et al. (2010a), ATMS NPP Preparation in the Community Radiative Transfer Model (CRTM): Spectral Response Function Analysis, in ITSC-17.
- van Delst, P., et al. (2010b), CRTM: ATMS NPP Spectral Response Function Analysis, JCSDA/EMC/SAIC, rev8775.
- Weng, F., X. Zou, X. Zou, N. Sun, H. Yang, M. Tian, W. J. Blackwell, X. Wang, L. Lin, and K. Anderson (2013), Calibration of Suomi national polar-orbiting partnership advanced technology microwave sounder, *J. Geophys. Res. Atmos.*, 118, 187–200, doi:10.1002/jgrd.50840.